

# Probing quadruplet scalar dark matter at current and future $pp$ colliders

Yu-Pan Zeng, Chengfeng Cai, Dan-Yang Liu, Zhao-Huan Yu,<sup>\*</sup> and Hong-Hao Zhang<sup>†</sup>  
*School of Physics, Sun Yat-Sen University, Guangzhou 510275, China*

We investigate a dark matter model involving an inert  $SU(2)_L$  quadruplet scalar with hypercharge  $1/2$ . After the electroweak symmetry breaking, the dark sector contains one doubly charged, two singly charged, and two neutral scalars. The lighter neutral scalar can be a viable dark matter candidate. Electroweak production of these scalars at the Large Hadron Collider leads to potential signals in the monojet +  $\cancel{E}_T$  and soft-leptons + jets +  $\cancel{E}_T$  channels. We thus derive constraints on the model by reinterpreting recent experimental searches. Based on simulation, we further evaluate the sensitivity at a future 100 TeV  $pp$  collider.

arXiv:1910.09431v2 [hep-ph] 25 Oct 2019

---

<sup>\*</sup> [yuzhaoh5@mail.sysu.edu.cn](mailto:yuzhaoh5@mail.sysu.edu.cn)

<sup>†</sup> [zh98@mail.sysu.edu.cn](mailto:zh98@mail.sysu.edu.cn)

**CONTENTS**

I. Introduction	3
II. Quadruplet scalar dark matter model	4
III. Relic abundance and direct detection	6
IV. Monojet searches at $pp$ colliders	8
A. LHC constraint	9
B. Sensitivity at a 100 TeV $pp$ collider	11
V. Soft-lepton searches at $pp$ colliders	12
A. LHC constraint	13
B. Sensitivity at a 100 TeV $pp$ collider	15
VI. Conclusions and discussions	18
Acknowledgments	19
A. Electroweak Gauge Interactions of the Quadruplet Scalar	20
References	21

## I. INTRODUCTION

Among various candidates of particle dark matter (DM), weakly interacting massive particles (WIMPs) seem rather appealing, because they could naturally predict a thermal relic abundance consistent with the observed value [1–3]. It is straightforward to construct WIMP models by extending the standard model (SM) with new colorless  $SU(2)_L$  multiplets in the dark sector [4–33], which have electroweak interaction strength by definition. The DM candidate in such models arises from the electrically neutral components of the multiplets.

If the DM candidate is a scalar particle, the minimal extension is to introduce an inert  $SU(2)_L$  doublet scalar with hypercharge  $Y = 1/2$  [34–37]. The term “inert” means that there exists an unbroken  $Z_2$  symmetry that forbids the doublet gaining a nonzero vacuum expectation value (VEV) and directly coupling to SM fermions. Consequently, if the lightest component of the doublet is one of the electrically neutral components, it would be stable, acting as a WIMP DM candidate. A next-to-minimal model can be constructed with an inert triplet scalar of  $Y = 0$  or  $Y = 1$  [38–42].

In this paper, we go further to study a scalar DM model with an inert quadruplet scalar of  $Y = 1/2$  [10, 19], which has been much less investigated in the past. There are three types of independent quartic couplings between the quadruplet and the SM Higgs doublet, which contribute to the mass terms of the quadruplet components due to the nonzero Higgs VEV. As a result, the components of the quadruplet are split in mass. Mass eigenstates in the dark sector include two neutral scalars, two singly charged scalars, and one doubly charged scalar. The lighter neutral scalar could be a viable DM candidate. Such a Quadruplet Scalar Dark Matter (QSDM) model could be well tested in experiments. DM scattering off nuclei can be mediated by the Higgs boson through the quartic couplings, leading to possible signals in direct detection experiments.

Moreover, the dark sector scalars could be produced in pairs at the Large Hadron Collider (LHC) via electroweak gauge interactions. Because of the  $Z_2$  symmetry, all these scalars finally decay into the DM particle, which can escape from the LHC detectors, resulting in a large missing transverse energy ( $\cancel{E}_T$ ) in the final state. Since the mass spectrum in the dark sector is typically compressed, visible decay products from the scalars tend to be soft. Therefore, a hard jet from initial state radiation may be required for triggering the signal at the LHC. Thus, one possible searching channel is the monojet +  $\cancel{E}_T$  channel, which has been widely applied for searching dark matter [43–48]. Furthermore, additional soft leptons may contain imprints of the scalar decays [49–53]. This motivates us to study a soft-leptons + jets +  $\cancel{E}_T$  channels well. We will estimate the related constraints on the QSDM model by reinterpreting the existed LHC searches.

At the LHC energies, electroweak production rates for the dark sector scalars are quite low, and hence the constraints from current LHC searches are still weak. Nevertheless, future  $pp$  colliders with much higher energies have been proposed, including the Super Proton-Proton Collider (SPPC) at  $\sqrt{s} \sim 70 - 100$  TeV [54] and the  $pp$  Future Circular Collider

(FCC-hh) at  $\sqrt{s} \sim 100$  TeV [55]. The increase of the collision energy makes it possible to probe much heavier electroweak scalars. We thus explore the sensitivity to the QSDM model at a 100 TeV  $pp$  collider based on Monte Carlo simulation.

This paper is organized as follows. In Sec. II, we introduce the model details. In Sec. III, we identify the parameter regions that is consistent with the observed relic abundance and study the constraints from direct detection experiments. In Sec. IV, we explore the constraint from the LHC search in the monojet +  $\cancel{E}_T$  channel, as well as the sensitivity at a 100 TeV  $pp$  collider. In Sec. V, the soft-leptons + jets +  $\cancel{E}_T$  channel is studied. Section VI gives the conclusions and discussions.

## II. QUADRUPLET SCALAR DARK MATTER MODEL

In the QSDM model, we introduce a  $SU(2)_L$  quadruplet scalar  $X$  with hypercharge  $Y = 1/2$  [10, 19]. We assume that  $X$  is inert, i.e.,  $X$  is odd under a  $Z_2$  symmetry, but all SM fields are  $Z_2$  even. On the one hand, we can express the quadruplet in the vector notation  $X = (X^{++}, X^+, X^0, X^-)^T$  with explicitly indicated electric charges. On the other hand, it can be denoted by a totally symmetric  $SU(2)_L$  tensor  $X^{ijk}$  ( $i, j, k = 1, 2$ ). The components in the two notations are related by

$$X = \begin{pmatrix} X^{++} \\ X^+ \\ X^0 \\ X^- \end{pmatrix} = \begin{pmatrix} X^{111} \\ \sqrt{3}X^{112} \\ \sqrt{3}X^{122} \\ X^{222} \end{pmatrix}. \quad (1)$$

Note that  $X^+ \neq (X^-)^*$ . The neutral component  $X^0$  can be separated into two real scalars  $\phi$  and  $a$ :

$$X^0 = \frac{1}{\sqrt{2}}(\phi + ia). \quad (2)$$

The Lagrangian in the QSDM model is given by

$$\mathcal{L} = \mathcal{L}_{\text{SM}} + (D_\mu X)^\dagger D^\mu X - V(X), \quad (3)$$

where  $\mathcal{L}_{\text{SM}}$  is the SM Lagrangian and  $V(X)$  is the potential involving  $X$ . The covariant derivative for  $X$  is  $D_\mu = \partial_\mu - igW_\mu^a T^a - ig'B_\mu/2$ , where  $T^a$  are the  $SU(2)_L$  generators in the representation 4. Electroweak gauge interaction terms for the quadruplet are explicitly given in Appendix A.

Respecting the  $Z_2$  symmetry  $X^{ijk} \rightarrow -X^{ijk}$ , we write down the potential  $V(X)$  as

$$V(X) = M_X^2 |X|^2 + \lambda_0 |X|^2 |H|^2 + \lambda_1 X_{ijk}^\dagger X^{ijl} H_l^\dagger H^k + (\lambda_2 X^{ikl} X^{jmn} H_i^\dagger H_j^\dagger \epsilon_{km} \epsilon_{ln} + \text{H.c.}) \\ + \text{self-interaction terms of } X, \quad (4)$$

where  $H$  is the SM Higgs doublet. Here we adopt a convention  $\epsilon^{12} = 1 = -\epsilon_{12}$  for the asymmetric tensors  $\epsilon^{ij}$  and  $\epsilon_{ij}$ . We do not give the explicit forms for the quadruplet self-interaction terms, because they will not affect the following discussions. Note that one may write down an extra operator  $X_{ijk}^\dagger X^{ijl} H_m^\dagger H^n \epsilon^{km} \epsilon_{ln}$ , but it is not independent because  $X_{ijk}^\dagger X^{ijl} H_m^\dagger H^n \epsilon^{km} \epsilon_{ln} = X_{ijk}^\dagger X^{ijl} H_l^\dagger H^k - |X|^2 |H|^2$ . If  $\lambda_2$  is complex, we can always make it real by a phase redefinition of the quadruplet. Hereafter we just use a real  $\lambda_2$ .

After  $H$  gets its VEV  $v = 246.22$  GeV, mass terms for the quadruplet components can be expressed as

$$\mathcal{L}_{\text{mass}} = -\frac{1}{2}m_\phi^2\phi^2 - \frac{1}{2}m_a^2a^2 - \left((X^+)^* \ X^-\right) M_C^2 \begin{pmatrix} X^+ \\ (X^-)^* \end{pmatrix} - m_{++}^2 |X^{++}|^2, \quad (5)$$

with

$$m_\phi^2 = M_X^2 + \frac{1}{6}(3\lambda_0 + 2\lambda_1 - 4\lambda_2)v^2, \quad (6)$$

$$m_a^2 = M_X^2 + \frac{1}{6}(3\lambda_0 + 2\lambda_1 + 4\lambda_2)v^2, \quad (7)$$

$$M_C^2 = \begin{pmatrix} M_X^2 + (3\lambda_0 + \lambda_1)v^2/6 & \lambda_2 v^2/\sqrt{3} \\ \lambda_2 v^2/\sqrt{3} & M_X^2 + (\lambda_0 + \lambda_1)v^2/2 \end{pmatrix}, \quad (8)$$

$$m_{++}^2 = M_X^2 + \frac{1}{2}\lambda_0 v^2. \quad (9)$$

The mass-squared matrix  $M_C^2$  for the singly charged scalars can be diagonalized by a  $2 \times 2$  rotation matrix  $O$ , which satisfies

$$O^T M_C^2 O = \begin{pmatrix} m_1^2 & \\ & m_2^2 \end{pmatrix}, \quad (10)$$

$$O = \begin{pmatrix} \cos \theta & -\sin \theta \\ \sin \theta & \cos \theta \end{pmatrix}. \quad (11)$$

The rotation angel  $\theta$  can be obtained from

$$\sin \theta = \frac{-\sqrt{6}\lambda_2}{\sqrt{\lambda_1^2 + 12\lambda_2^2 + \lambda_1\sqrt{\lambda_1^2 + 12\lambda_2^2}}}. \quad (12)$$

Thus, the singly charged mass eigenstates  $X_1^+$  and  $X_2^+$  are related to the gauge eigenstates  $X^+$  and  $(X^-)^*$  through

$$\begin{pmatrix} X^+ \\ (X^-)^* \end{pmatrix} = O \begin{pmatrix} X_1^+ \\ X_2^+ \end{pmatrix}. \quad (13)$$

Their masses squared are given by

$$m_1^2 = M_X^2 + \frac{v^2}{12} \left( 6\lambda_0 + 4\lambda_1 - 2\sqrt{\lambda_1^2 + 12\lambda_2^2} \right), \quad (14)$$

$$m_2^2 = M_X^2 + \frac{v^2}{12} \left( 6\lambda_0 + 4\lambda_1 + 2\sqrt{\lambda_1^2 + 12\lambda_2^2} \right). \quad (15)$$

The mass hierarchy of the neutral scalars  $\phi$  and  $a$  is determined by the sign of  $\lambda_2$ . If  $\lambda_2 > 0$  ( $\lambda_2 < 0$ ),  $\phi$  is lighter (heavier) than  $a$ , and thus  $\phi$  ( $a$ ) is a possible DM candidate. Nevertheless, if  $|\lambda_1| > 2|\lambda_2|$ , one of the singly charged scalars is lighter than the DM candidate. Additionally, if  $\lambda_1 > 2|\lambda_2|$ , the doubly charged scalar is lighter than the DM candidate. Since the DM candidate should be the lightest particle in the dark sector for ensuring its stability, we have the following conclusions.

- If  $\lambda_2 > 0$  and  $|\lambda_1| \leq 2\lambda_2$ , then  $\phi$  is a viable DM candidate.
- If  $\lambda_2 < 0$  and  $|\lambda_1| \leq -2\lambda_2$ , then  $a$  is a viable DM candidate.

The model has two kinds of  $CP$  symmetries, one with  $\phi \rightarrow \phi$  and  $a \rightarrow -a$ , and the other one with  $\phi \rightarrow -\phi$  and  $a \rightarrow a$ . A transformation  $X^{ijk} \rightarrow iX^{ijk}$  and  $\lambda_2 \rightarrow -\lambda_2$  can keep the Lagrangian unchanged, but interchange the two  $CP$  symmetries and hence the roles of  $\phi$  and  $a$  [56]. Therefore, we know that  $\phi$  and  $a$  have opposite  $CP$  parities, but it is impossible to determine their absolute  $CP$  parities without additional interactions. Without loss of generality, hereafter we adopt  $\lambda_2 > 0$  and take  $\phi$  as the DM candidate. The resulting discussions are totally equivalent to those for  $\lambda_2 < 0$  and  $a$  as the DM candidate.

### III. RELIC ABUNDANCE AND DIRECT DETECTION

In this section, we evaluate the relic abundance prediction in the QSDM model, and investigate the constraints from direct detection experiments.

The dark sector scalars can interact with SM particles via electroweak gauge couplings and scalar couplings to the Higgs boson. Through such interactions, these scalars could be thermally produced in the early Universe, and decoupled from the cosmic plasma at the freeze-out epoch. Conventionally, the relic abundance of dark matter is determined by the its freeze-out annihilation cross section. Nonetheless, for  $m_X \sim \mathcal{O}(\text{TeV})$ , the mass splittings among the dark sector scalars due to the quartic couplings would be relatively small, and thus the scalars actually freeze out around the same epoch. Therefore, the coannihilation effect would be significant for evaluating the relic abundance [57].

We utilize a few numerical tools to predict the relic abundance of the DM candidate  $\phi$ . `FeynRules 2` [58] is adopted to implement the QSDM model, interfaced to the Monte Carlo generator `MadGraph5_aMC@NLO 2` [59]. The relic abundance  $\Omega_\phi h^2$  is calculated by a `MadGraph` plugin `MadDM` [60], which can reliably take into account the coannihilation effect.

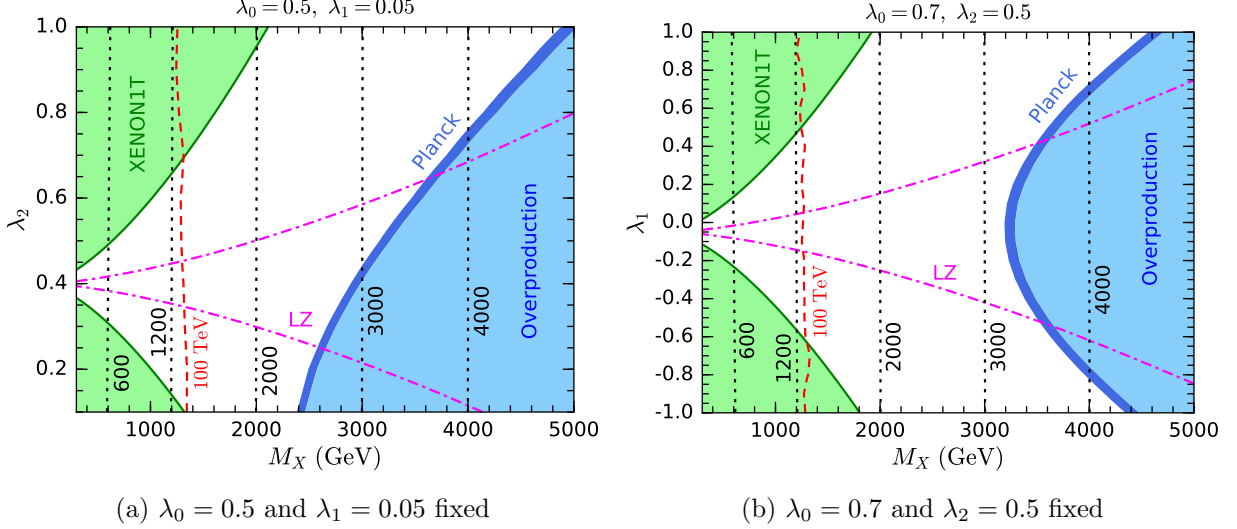


FIG. 1. Experimental constraints and sensitivities in the  $M_X$ - $\lambda_2$  (a) and  $M_X$ - $\lambda_1$  (b) planes. The black dotted lines denote the DM candidate mass  $m_\phi$  in GeV. The blue bands correspond to the  $3\sigma$  range of the Planck relic abundance measurement [61], while the light blue regions predict overproduction of dark matter. The green regions are excluded by the direct detection experiment XENON1T [62]. The dashed magenta lines indicate the exclusion capability of the future direct detect experiment LZ [63]. The dashed red lines show the exclusion capability of the monojet +  $\cancel{E}_T$  channel at a 100 TeV  $pp$  collider with a data set of  $3 \text{ ab}^{-1}$  (see Sec. IV).

The measurement of the DM relic abundance in the Planck experiment gives  $\Omega_{\text{DM}} = 0.1200 \pm 0.0012$  [61]. In Figs. 1(a) and 1(b), we fix the parameters  $(\lambda_0, \lambda_1) = (0.5, 0.05)$  and  $(\lambda_0, \lambda_2) = (0.7, 0.5)$  and show the parameter regions that are consistent with the Planck observation as the blue bands in the  $M_X$ - $\lambda_2$  and  $M_X$ - $\lambda_1$  planes, respectively. The black dotted lines indicate the contours of the DM candidate mass  $m_\phi$ , which slightly deviates from  $M_X$  due to the quartic couplings.

If  $M_X$  increases, the effective annihilation cross section typically decreases, leading to an increase in the relic abundance. Therefore, the light blue regions with large  $M_X$  predict overproduction of  $\phi$  particles in the early Universe, which contradicts standard cosmology. For small values of  $\lambda_2$  ( $|\lambda_1|$ ) in Fig. 1(a) (Fig. 1(b)), the relic abundance observation corresponds to  $M_X \sim 2.4$  (3.3) TeV, which increases to  $M_X \sim 5$  (4.6) TeV when  $\lambda_2$  ( $|\lambda_1|$ ) increases to one.

Direct detection experiments look for signals of DM scattering off nuclei. In the QSDM model, DM scattering is mediated by the Higgs boson  $h$ , arising from the quartic potential terms that lead to the  $h\phi\phi$  interaction Lagrangian

$$\mathcal{L}_{h\phi\phi} = \frac{1}{2}\lambda_{h\phi\phi}vh\phi^2, \quad (16)$$

$$\lambda_{h\phi\phi} = -\lambda_0 - \frac{2}{3}\lambda_1 + \frac{4}{3}\lambda_2. \quad (17)$$

As direct detection experiments basically operate at zero momentum transfer, the interactions between DM and quarks can be described by dimension-5 effective operators [64]. As a result, the spin-independent DM-nucleon scattering cross section can be expressed as

$$\sigma_{\chi N}^{\text{SI}} = \frac{m_N^2 F_N^2}{4\pi(m_\phi + m_N)^2}, \quad N = p, n, \quad (18)$$

where

$$F_N = -\frac{\lambda_{h\phi\phi} m_N}{9m_h^2} [2 + 7(f_u^N + f_d^N + f_s^N)]. \quad (19)$$

Here the nucleon form factors  $f_q^N$  are given by [65]

$$\begin{aligned} f_u^p &= 0.020 \pm 0.004, & f_d^p &= 0.026 \pm 0.005, & f_u^n &= 0.014 \pm 0.003, \\ f_d^n &= 0.036 \pm 0.008, & f_s^p &= f_s^n &= 0.118 \pm 0.062. \end{aligned} \quad (20)$$

In Figs. 1(a) and 1(b), we show the parameter regions excluded by the direct detection experiment XENON1T [62] at 90% confidence level (C.L.). According to Eq. (17), we can take some particular relations among  $\lambda_0$ ,  $\lambda_1$ , and  $\lambda_2$  to give a vanishing  $h\phi\phi$  coupling, resulting in “blind spots” for direct detection experiments. For Figs. 1(a) and 1(b), the limits  $\lambda_2 = 3\lambda_0/4 + \lambda_1/2 = 0.4$  and  $\lambda_1 = -3\lambda_0/2 + 2\lambda_2 = -0.05$  correspond to  $\lambda_{h\phi\phi} = 0$ , respectively. Therefore, direct detection experiments lose their sensitivities as  $\lambda_2$  or  $\lambda_1$  approaches the corresponding limit. Nonetheless, the XENON1T experiment has excluded some disconnected parameter regions with  $M_X \lesssim 1.3 - 2$  TeV. We also demonstrate the expected 90% C.L. exclusion limits of the future direct detection experiment LZ [63], which will explore the parameter space much deeper and be able to reach the regions suggested by the relic abundance measurement.

#### IV. MONOJET SEARCHES AT $pp$ COLLIDERS

Through the electroweak gauge couplings, the dark sector scalars in the QSDM model could be directly produced in pairs at the LHC. The corresponding processes can be expressed as  $pp \rightarrow \chi_i \chi_j + \text{jets}$  with  $\chi_i = (\phi, a, X_1^\pm, X_2^\pm, X^{\pm\pm})$ . After production, a heavier scalar  $\chi_k$  may decay into a lighter scalar  $\chi_l$  via  $\chi_k \rightarrow W^{\pm(*)}/Z^{(*)}/h^{(*)} + \chi_l$ . Depending on the mass splitting between  $\chi_k$  and  $\chi_l$ , the produced  $W^\pm$ ,  $Z$ , and  $h$  bosons can be either on or off shell. Subsequent decays may happen and form decay chains. Finally, all  $Z_2$ -odd scalars will decay into the DM candidate  $\phi$ , which is stable and escape from detection, leading to a large  $\cancel{E}_T$ .

Figure 2 shows the mass splittings between  $(a, X_1^\pm, X_2^\pm, X^{\pm\pm})$  and  $\phi$  as functions of  $M_X$  for  $\lambda_0 = 0.1$  and  $\lambda_1 = \lambda_2 = 0.2$ . From this plot, we can read off the mass difference between each pair of dark sector scalars. As  $M_X$  increases, the contributions from the quartic couplings relatively decrease, resulting in smaller splittings. The mass splitting

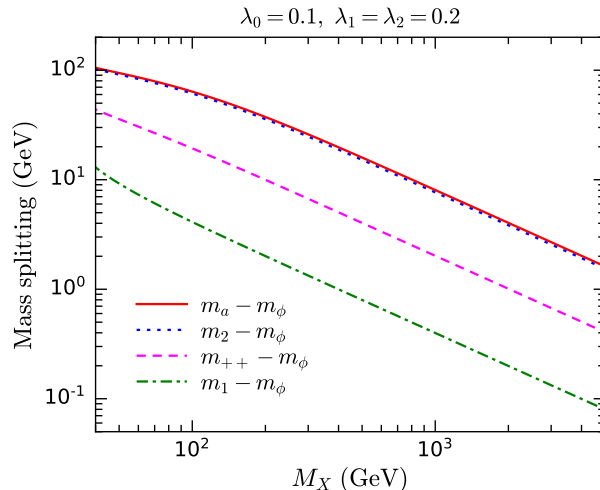


FIG. 2. Mass splittings as functions of  $M_X$  for  $\lambda_0 = 0.1$  and  $\lambda_1 = \lambda_2 = 0.2$ .

between the two neutral scalars  $a$  and  $\phi$  is the largest one, ranging from  $\sim 100$  to  $\sim 2$  GeV as  $m_X$  increases from 40 GeV to 5 TeV. For  $m_X \gtrsim 70$  GeV, the splittings are not large enough to induce on-shell  $W^\pm$ ,  $Z$ , or  $h$  bosons. For fixed  $M_X$ , smaller quartic couplings would further compress the mass spectrum.

In the above analysis, we find that the mass splittings in the QSDM model are typically small. Consequently, visible decay products from the dark sector scalars would be quite soft and hence difficult to be triggered in detectors. In order to effectively trigger the signal, we can require at least one hard jet from initial state radiation to recoil the  $\chi_i\chi_j$  pair, leading to a monojet +  $\cancel{E}_T$  final state [43–45]. SM backgrounds in the monojet +  $\cancel{E}_T$  search channel include two major backgrounds,  $W(\rightarrow l\nu) + \text{jets}$  and  $Z(\rightarrow \nu\bar{\nu}) + \text{jets}$ , and some minor backgrounds, such as  $t\bar{t} + \text{jets}$  and  $VV + \text{jets}$  ( $V = W^\pm, Z$ ). In these backgrounds,  $\cancel{E}_T$  mainly arises from neutrinos in the decay products.

### A. LHC constraint

In this subsection, we investigate the current LHC constraint on the QSDM model by reinterpreting the ATLAS analysis in the monojet +  $\cancel{E}_T$  channel with an integrated luminosity of  $36.1 \text{ fb}^{-1}$  at  $\sqrt{s} = 13 \text{ TeV}$  [66]. For this purpose, we utilize **MadGraph** [59] to generate signal simulation samples. Parton shower is performed by **PYTHIA 8** [67] with the MLM matching scheme [68]. **PYTHIA** is also carried out for hadronization and decay processes. Then we use **Delphes 3** [69] for a fast detector simulation with a setup for the ATLAS detector.

We simulate the signal processes  $pp \rightarrow \chi_i\chi_j + \text{jets}$  and apply the same selection cuts in the ATLAS analysis [66] to the simulation events. Isolated leptons, including electrons and muons, and jets are reconstructed with the conditions on  $p_T$  and  $\eta$  listed in Table I. Then the

TABLE I. Reconstruction and cut conditions in the monojet +  $\cancel{E}_T$  channel.

	13 TeV LHC	100 TeV $pp$ collider
Reconstruction conditions		
Electron $p_T,  \eta $	$> 20 \text{ GeV}, < 2.47$	$> 40 \text{ GeV}, < 2.47$
Muon $p_T,  \eta $	$> 10 \text{ GeV}, < 2.5$	$> 20 \text{ GeV}, < 2.5$
Jet $p_T,  \eta $	$> 30 \text{ GeV}, < 2.8$	$> 60 \text{ GeV}, < 2.8$
Cut conditions		
Number of leptons	0	0
Leading jet $p_T,  \eta $	$> 250 \text{ GeV}, < 2.4$	$> 1.4 \text{ TeV}, < 2.4$
Number of jets	$\leq 4$	$\leq 4$
$\Delta\phi(j_i, \cancel{\mathbf{p}}_T)$	$> 0.4$	$> 0.4$
$\cancel{E}_T$	$> 250 - 1000 \text{ GeV}$	$> 1.5 - 2.8 \text{ TeV}$

events in the signal regions are required to have a hard leading jet with  $p_T > 250 \text{ GeV}$  and  $|\eta| < 2.4$  and a missing transverse energy  $\cancel{E}_T$  at least larger than  $250 \text{ GeV}$ . In addition, there should be no leptons and no more than four jets. Moreover, the separation in the azimuthal angle between any reconstructed jet  $j_i$  and the missing transverse momentum  $\cancel{\mathbf{p}}_T$  should satisfy  $\Delta\phi(j_i, \cancel{\mathbf{p}}_T) > 0.4$  for preventing a large  $\cancel{E}_T$  from mismeasurement of jets. Finally, ten inclusive and ten exclusive signal regions are defined with different  $\cancel{E}_T$  thresholds, whose explicit definitions can be found in Table 1 of Ref. [66]. In Table I, we summarize the cut conditions above.

Based on the signal simulation samples, we estimate the visible cross section in each signal region, which is a product of production cross section, acceptance, and efficiency, and then use the 95% C.L. observed experimental upper limit to derive constraints on the QSDM model. Taking into account all the signal regions, the combined exclusion region in the  $m_\phi$ - $\lambda_2$  plane is shown in Fig. 3(a), where we fix a coupling relation of  $\lambda_1 = \lambda_2 = 3\lambda_0/2$ . Because of Eq. (17), such a relation leads to  $\lambda_{h\phi\phi} = 0$ , and there is no constraint from direct detection experiments. Therefore, collider searches are really important in this case. Note that  $\lambda_{h\phi\phi} = 0$  also leads to  $m_\phi = m_X$ , according to Eqs. (6) and (17). We find that the monojet search has excluded a region with  $m_\phi \lesssim 33 \text{ GeV}$  and  $\lambda_2 \lesssim 0.3$ . Nonetheless, the sensitivity decreases as  $\lambda_2$  increases. The reason is that a larger  $\lambda_2$  leads to larger mass splittings among the dark sector scalars and hence harder leptons from scalar decays that would not be easy to pass the cuts.

In Fig. 3(b), we adopt another relation  $\lambda_0 = 0$  and  $\lambda_1 = 2\lambda_2$ , which also results in  $\lambda_{h\phi\phi} = 0$ . Additionally, it leads to degenerate mass spectra with  $m_\phi = m_1 = m_{++}$  and  $m_a = m_2$ . Consequently, many decay channels are turned off, significantly reducing the probability of finding leptons in the final state. Therefore, the monojet search is more sensitive, excluding a region up to  $m_\phi \sim 45 \text{ GeV}$ . The exclusion is basically regardless of

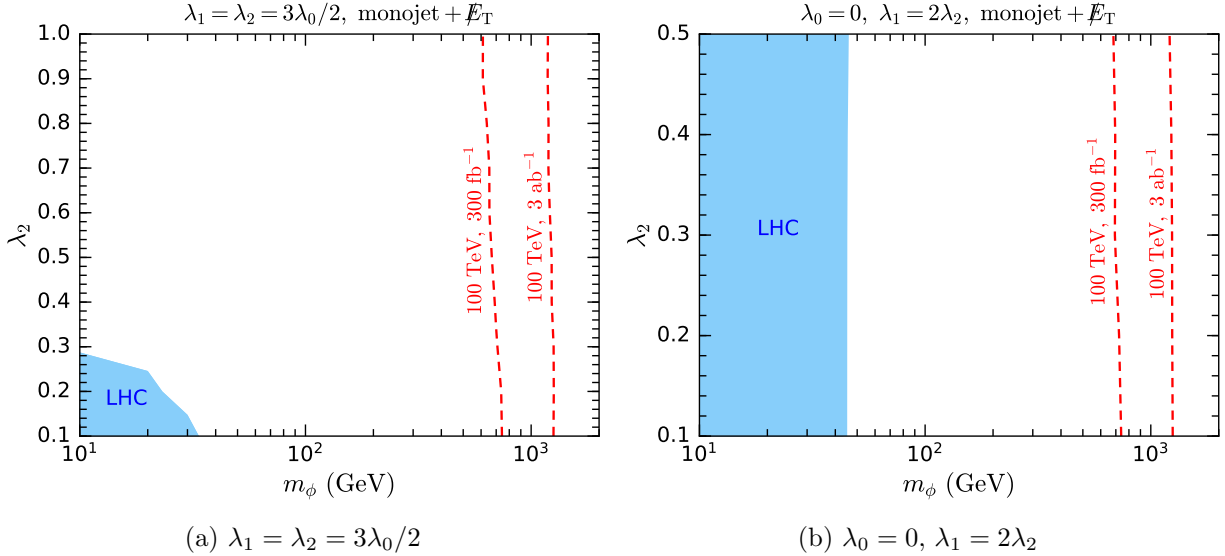


FIG. 3. Current constraints and future sensitivities from the monojet +  $\cancel{E}_T$  channel in the  $m_\phi$ - $\lambda_2$  plane for the fixed coupling relations of  $\lambda_1 = \lambda_2 = 3\lambda_0/2$  (a) and of  $\lambda_0 = 0$  and  $\lambda_1 = 2\lambda_2$  (b). The blue regions are excluded at 95% C.L. by the ATLAS search with a  $36.1 \text{ fb}^{-1}$  data set at the 13 TeV LHC [66]. The red dashed lines denote the 95% C.L. expected exclusion limits at a 100 TeV  $pp$  collider with integrated luminosities of  $300 \text{ fb}^{-1}$  and  $3 \text{ ab}^{-1}$ .

the  $\lambda_2$  value.

## B. Sensitivity at a 100 TeV $pp$ collider

The above results have shown that the current LHC monojet search is rather insensitive to the QSDM model, just probing a scale of a few tens of GeV. Since production cross sections in  $pp$  collisions typically increase as  $\sqrt{s}$  increases, we expect that monojet searches at a future  $pp$  collider with  $\sqrt{s} \sim 100$  TeV would be much more sensitive. Below we estimate the projected sensitivity in the monojet +  $\cancel{E}_T$  channel at a 100 TeV  $pp$  collider based on simulation. The obtained results would be applicable to both the SPCC and FCC-hh projects.

In the simulation with  $\sqrt{s} = 100$  TeV, we consider the signal processes and only the primary SM backgrounds  $W (\rightarrow l\nu) + \text{jets}$  and  $Z (\rightarrow \nu\bar{\nu}) + \text{jets}$ . Other backgrounds should be small and can be safely neglected. In the Delphes simulation, we conservatively assume that the future detector has the same parameters as those in the ATLAS detector. The thresholds in the reconstruction and cut conditions are appropriately adjusted for a 100 TeV  $pp$  collider, as also demonstrated in Table I.

Four signal regions are defined by requiring  $\cancel{E}_T > 1.5, 1.8, 2.2, 2.8$  TeV. In each signal

region, the signal significance  $\mathcal{S}$  is defined as

$$\mathcal{S} = \frac{S}{\sqrt{S+B}}, \quad (21)$$

where  $S$  and  $B$  are the estimated numbers of the signal events and the total background events passing the corresponding cuts, respectively. The expected exclusion limits at 95% C.L. are also shown in Figs. 3(a) and 3(b). For data sets of  $300 \text{ fb}^{-1}$  and  $3 \text{ ab}^{-1}$  at  $\sqrt{s} = 100 \text{ TeV}$ , monojet searches are expected to probe the DM candidate mass  $m_\phi$  up to  $\sim 700 \text{ GeV}$  and  $\sim 1.2 \text{ TeV}$ , respectively. Thus, a 100 TeV  $pp$  collider looks much more powerful than the LHC.

In order to compare with direct detection and relic abundance observation, we have also plotted the 95% C.L. expected exclusion limits in monojet +  $\cancel{E}_T$  channel at  $\sqrt{s} = 100 \text{ TeV}$  with an integrated luminosity of  $3 \text{ ab}^{-1}$  in Figs. 1(a) and 1(b). We find that the 100 TeV monojet searches could cover some regions where direct detection experiments cannot probe. Nonetheless, the regions predicting an observed relic abundance could not be reached.

## V. SOFT-LEPTON SEARCHES AT $pp$ COLLIDERS

Besides the monojet channel, leptons arising from the scalar decays  $\chi_i \rightarrow \chi_j + W^{\pm(*)}(\rightarrow \ell^\pm \nu_\ell)/Z^{(*)}(\rightarrow \ell^\pm \ell^\mp)$  may also contain important information for exploring the QSDM model. Inspired by the searches for electroweak production of charginos and neutralinos in supersymmetric models, we firstly consider the final states involving two or three ‘‘hard’’ leptons. After recasting the related ATLAS analysis at  $\sqrt{s} = 13 \text{ TeV}$  with a data set of  $36.1 \text{ fb}^{-1}$  [70], however, we do not find any meaningful constraint on the QSDM model. The main reason is that the leptons from the scalar decays tend to be rather soft, because the mass spectrum is typically compressed, as explained in the previous section.

Therefore, it is more suitable to consider the final states with ‘‘soft’’ leptons. In this case, a pair of same-flavor opposite-sign (SFOS) soft leptons with an invariant mass  $\lesssim 60 \text{ GeV}$  could lead to a distinct signature [52, 53]. In the signal process  $pp \rightarrow \chi_i \chi_j + \text{jets}$ , such a SFOS lepton pair may come from the scalar decays into an off-shell  $Z$  boson. In order to induce a sufficiently large  $\cancel{E}_T$ , a hard jet with a transverse direction roughly opposite to that of  $\mathbf{p}_T$  is also required. Such a soft-leptons + jets +  $\cancel{E}_T$  channel has been utilized in the ATLAS search for supersymmetric particles with compressed mass spectra at the 13 TeV LHC with an integrated luminosity of  $36.1 \text{ fb}^{-1}$  [71]. Important SM backgrounds in this channel include  $t\bar{t} + \text{jets}$ ,  $tW + \text{jets}$ ,  $VV + \text{jets}$ , and  $\tau^+\tau^- + \text{jets}$ .

TABLE II. Reconstruction and cut conditions in the ATLAS soft-leptons + jets +  $\cancel{E}_T$  analysis at  $\sqrt{s} = 13$  TeV [71].

Reconstruction conditions	
Electron $p_T,  \eta $	$> 4.5$ GeV, $< 2.47$
Muon $p_T,  \eta $	$> 4$ GeV, $< 2.5$
Non- $b$ -tagged jet $p_T,  \eta $	$> 30$ GeV, $< 2.8$
$b$ -tagged jet $p_T,  \eta $	$> 20$ GeV, $< 2.5$
Cut conditions	
Number of leptons	2
Lepton flavor and charge	$e^+e^-$ or $\mu^+\mu^-$
Leading lepton $p_T^{\ell_1}$	$> 5$ GeV
Subleading lepton $p_T^{\ell_2}$	$> 4.5$ (4) GeV for $\ell_2 = e$ ( $\mu$ )
$\Delta R_{\ell\ell}$	$0.05 < \Delta R_{\ell\ell} < 2$
$m_{\ell\ell}$	$[1, 3] \cup [3.2, 60]$ GeV
$\cancel{E}_T$	$> 200$ GeV
Number of jets	$\geq 1$
Leading jet $p_T$	$> 100$ GeV
$\Delta\phi(j_1, \cancel{\mathbf{p}}_T)$	$> 2$
$\min(\Delta\phi(j_i, \cancel{\mathbf{p}}_T))$	$> 0.4$
Number of $b$ -tagged jets	0
$m_{\tau\tau}$	$< 0$ or $> 160$ GeV
$m_T^{\ell_1}$	$< 70$ GeV
$\cancel{E}_T/H_T^{\text{lep}}$	$> \max(5, 15 - 2m_{\ell\ell}/\text{GeV})$

### A. LHC constraint

We reinterpret the ATLAS analysis [71] to study the current constraint on the QSDM model in the soft-leptons + jets +  $\cancel{E}_T$  channel. The corresponding reconstruction and cut conditions are summarized in Table II. The  $p_T$  thresholds for reconstructed electrons and muons are lowered to 4.5 and 4 GeV for keeping “soft” leptons in the final state. There should be exact two leptons forming a SFOS pair, whose direction distance  $\Delta R_{\ell\ell}$  and invariant mass  $m_{\ell\ell}$  should lie in proper ranges because they are considered to be originated from an off-shell  $Z$  boson. Events with  $m_{\ell\ell} \in (3, 3.2)$  GeV are rejected to avoid contamination from  $J/\psi$  decays. In order to increase the signal-to-background ratio, at least one jet with  $p_T > 100$  GeV and  $\cancel{E}_T > 200$  GeV are required. The condition  $\Delta\phi(j_1, \cancel{\mathbf{p}}_T) > 2$  is used to ensure the transverse directions of the leading jet and  $\cancel{\mathbf{p}}_T$  are quite opposite. In order to suppress the  $t\bar{t}$  + jets and  $tW$  + jets backgrounds, no  $b$ -tagged jet is allowed.

For further increasing the signal significance, some dedicated kinematic variables are utilized. The  $m_{\tau\tau}$  variable [52, 53, 71, 72] constructed by the SFOS lepton pair is help-

TABLE III. Signal regions defined by the  $m_{\ell\ell}$  bins in the ATLAS soft-leptons + jets +  $\cancel{E}_T$  analysis at  $\sqrt{s} = 13$  TeV [71].

Signal regions	SR1	SR2	SR3	SR4	SR5	SR6	SR7
$m_{\ell\ell}$ (GeV)	[1,3]	[1,5]	[1,10]	[1,20]	[1,30]	[1,40]	[1,60]
$\sigma_{\text{vis}}^{\text{obs}}$ (fb)	0.10	0.18	0.34	0.61	0.59	0.72	0.80

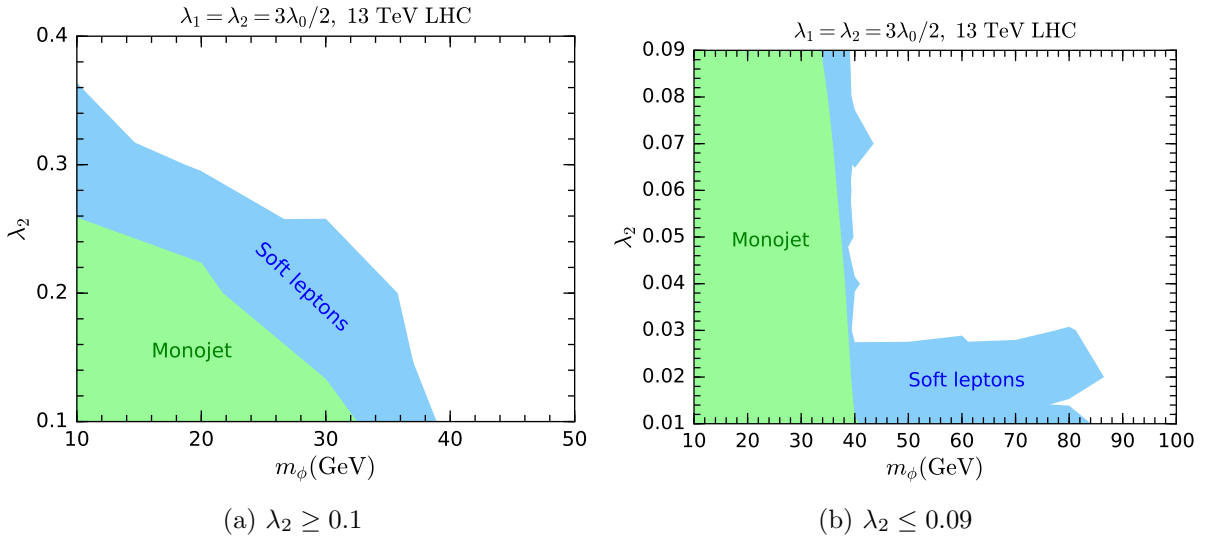


FIG. 4. Constraints from current LHC searches in the  $m_\phi$ - $\lambda_2$  plane with the fixed coupling relation  $\lambda_1 = \lambda_2 = 3\lambda_0/2$  for  $\lambda_2 \geq 0.1$  (a) and  $\lambda_2 \leq 0.09$  (b). Blue (green) regions are excluded at 95% C.L. by the ATLAS soft-leptons + jets +  $\cancel{E}_T$  [71] (monojet +  $\cancel{E}_T$  [66]) analysis at the 13 TeV LHC with a data set of  $36.1 \text{ fb}^{-1}$ .

ful for reducing the  $\tau^+\tau^- + \text{jets}$  background. The leading lepton transverse mass  $m_T^{\ell_1} = \sqrt{2(E_T^{\ell_1} \cancel{E}_T - \mathbf{p}_T^{\ell_1} \cdot \mathbf{p}_T)}$  is required to satisfy  $m_T^{\ell_1} < 70$  GeV, in order to suppress the  $t\bar{t} + \text{jets}$ ,  $VV + \text{jets}$ , and  $W + \text{jets}$  backgrounds. The ratio of  $\cancel{E}_T$  to the scalar sum of the transverse momenta of the leptons  $H_T^{\text{lep}} = p_T^{\ell_1} + p_T^{\ell_2}$  is used to improve the signal-to-background discrimination for compressed spectra.

We find that seven signal regions in the ATLAS analysis [71] could be sensitive to the QSDM model. They are defined with different inclusive  $m_{\ell\ell}$  bins, as tabulated in Table III. Note that the (3, 3.2) GeV interval has also removed in these bins. We also list the corresponding 95% C.L. observed limits on the visible cross section,  $\sigma_{\text{vis}}^{\text{obs}}$ . We thus simulate signal samples and apply the above cuts to obtain 95% C.L. exclusion limits on the QSDM model.

The exclusion regions from the seven signal regions are combined, shown as the blue regions in Fig. 4. The fixed coupling relation in Figs. 4(a) and 4(b) is identical to that in Fig. 3(a). For comparison, we also demonstrate the green regions excluded by the ATLAS monojet search, which has been discussed in the previous section. We find that the soft-leptons + jets +  $\cancel{E}_T$  channel is more sensitive than the monojet +  $\cancel{E}_T$  channel at

TABLE IV. Information of the four benchmark points with the fixed coupling relation  $\lambda_1 = \lambda_2 = 3\lambda_0/2$  in the QSDM model.

	$M_X/\text{GeV}$	$\lambda_2$	$m_{++}/\text{GeV}$	$m_\phi/\text{GeV}$	$m_a/\text{GeV}$	$m_1/\text{GeV}$	$m_2/\text{GeV}$
BMP1	400	0.2	405.0	400	419.7	401.0	418.7
BMP2	400	0.4	410.0	400	438.5	402.0	436.7
BMP3	500	0.2	504.0	500	515.9	500.8	515.1
BMP4	200	0.4	219.2	200	268.8	203.9	265.9

$\sqrt{s} = 13$  TeV. In Fig. 4(a) for  $\lambda_2 \geq 0.1$ , the soft-lepton search has excluded a region with  $m_\phi \lesssim 39$  GeV. In Fig. 4(b), we focus on the small  $\lambda_2$  region ( $\lambda_2 \leq 0.09$ ) and find that the soft-lepton search can probe up to  $m_\phi \sim 85$  GeV for  $\lambda_2 \lesssim 0.03$ . The reason is that the  $\cancel{E}_T/H_T^{\text{lep}}$  cut is more suitable for small mass splittings, say  $m_a - m_\phi \lesssim 20$  GeV, which is realized in such a  $\lambda_2 \lesssim 0.03$  region.

### B. Sensitivity at a 100 TeV $pp$ collider

In this subsection, we explore the soft-leptons+jets+ $\cancel{E}_T$  channel at a 100 TeV  $pp$  collider. The main backgrounds  $t\bar{t}$ +jets,  $tW$ +jets,  $VV$ +jets, and  $\tau^+\tau^-$ +jets are taken into account. In order to demonstrate a detailed study, we choose four benchmark points (BMPs) for the QSDM model with the fixed coupling relation  $\lambda_1 = \lambda_2 = 3\lambda_0/2$ , which leads to  $\lambda_{h\phi\phi} = 0$  and  $m_\phi = m_X$ . The parameters and mass spectra of the BMPs are displayed in Table IV. BMP1 and BMP2 have identical  $M_X$  and different  $\lambda_2$ , and thus a large  $\lambda_2$  leads to larger mass splittings. If  $\lambda_2$  is fixed, a larger  $M_X$  gives smaller mass splittings. This can be seen by comparing BMP3 to BMP1 or BMP4 to BMP2.

For a  $pp$  collider at  $\sqrt{s} = 100$  TeV, we adopt the following reconstruction conditions with higher  $p_T$  thresholds than those used at the LHC.

- Reconstructed electrons are required to have  $p_T > 10$  GeV and  $|\eta| < 2.47$  ;
- Reconstructed muons are required to have  $p_T > 10$  GeV and  $|\eta| < 2.5$ ;
- Reconstructed non- $b$ -tagged jets are required to have  $p_T > 60$  GeV and  $|\eta| < 2.8$ ;
- Reconstructed  $b$ -tagged jets are required to have  $p_T > 40$  GeV and  $|\eta| < 2.5$ .

We appropriately modify the cut conditions according to a collision energy of 100 TeV. They are classified into six subsequent cuts, as tabulated in Table V. The  $m_T^{\ell_1}$  cut is abandoned as we find that it would not be helpful.

Cut 1 selects the events with a proper soft SFOS lepton pair. After applying cut 1, the fraction of events binned in the leading jet  $p_T$  for the four BMPs and for the backgrounds  $t\bar{t}$ +jets,  $tW$ +jets,  $VV$ +jets, and  $\tau^+\tau^-$ +jets are presented in Fig. 5(a). We can see that

TABLE V. Cut conditions in the soft-leptons + jets +  $\cancel{E}_T$  channel at a 100 TeV  $pp$  collider.

Cut 1	Exact two SFOS leptons Leading lepton $p_T > 12$ GeV, $0.05 < \Delta R_{\ell\ell} < 2$
Cut 2	At least one jet, no $b$ -tagged jet Leading jet $p_T > 200$ GeV $\Delta\phi(j_1, \cancel{\mathbf{p}}_T) > 2.0$ , $\min(\Delta\phi(j_i, \cancel{\mathbf{p}}_T)) > 0.4$
Cut 3	$m_{\tau\tau} < 0$ or $m_{\tau\tau} > 200$ GeV
Cut 4	$\cancel{E}_T > 280$ GeV
Cut 5	$\cancel{E}_T/H_T^{\text{lep}} > \max(5, 15 - 2m_{\ell\ell}/\text{GeV})$
Cut 6	$m_{\ell\ell} \in [1, 3] \cup [3.2, 60]$ GeV

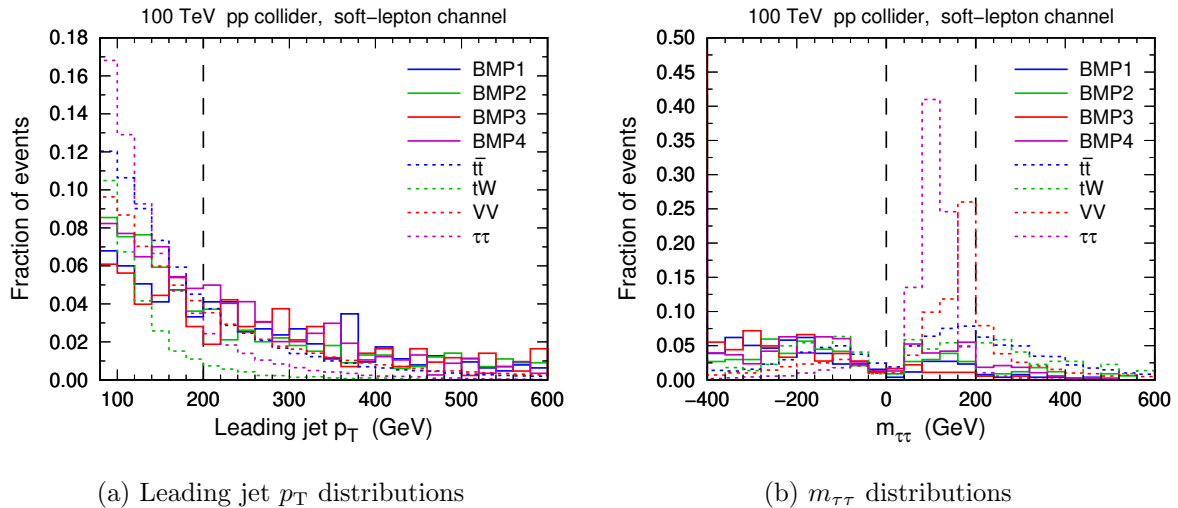


FIG. 5. Fraction of signal and background events binned in the leading jet  $p_T$  after cut 1 (a) and in  $m_{\tau\tau}$  after cut 2 (b) in the soft-leptons + jets +  $\cancel{E}_T$  channel at a 100 TeV  $pp$  collider. Dashed lines indicate the cut thresholds.

these backgrounds tend to have lower  $p_T$ . Thus, we require the leading jet  $p_T > 200$  GeV in cut 2 for reducing the backgrounds.

Figure 5(b) shows the  $m_{\tau\tau}$  distributions of signal and background events after cut 2. The  $m_{\tau\tau}$  variable is defined by  $m_{\tau\tau} = \text{sign}(m_{\tau\tau}^2)\sqrt{|m_{\tau\tau}^2|}$  with  $m_{\tau\tau}^2 \equiv (1 + \xi_1)(1 + \xi_2)m_{\ell\ell}^2$ , where  $\xi_1$  and  $\xi_2$  are parameters determined by solving  $\cancel{\mathbf{p}}_T = \xi_1\mathbf{p}_T^{\ell_1} + \xi_2\mathbf{p}_T^{\ell_2}$  event by event [52, 53, 71, 72]. If the  $\tau$  leptons in the  $pp \rightarrow Z^{(*)}/\gamma^*(\rightarrow \tau^+\tau^-) + \text{jets}$  process both decay leptonically and the daughter neutrinos are collinear with the daughter charged leptons, such a  $m_{\tau\tau}$  definition will truly correspond to the invariant mass of the  $\tau$  leptons when the missing transverse momentum  $\cancel{\mathbf{p}}_T$  are genuinely contributed by the neutrinos. Such a collinear situation would be realized when the two  $\tau$  leptons are sufficiently boosted. Consequently,

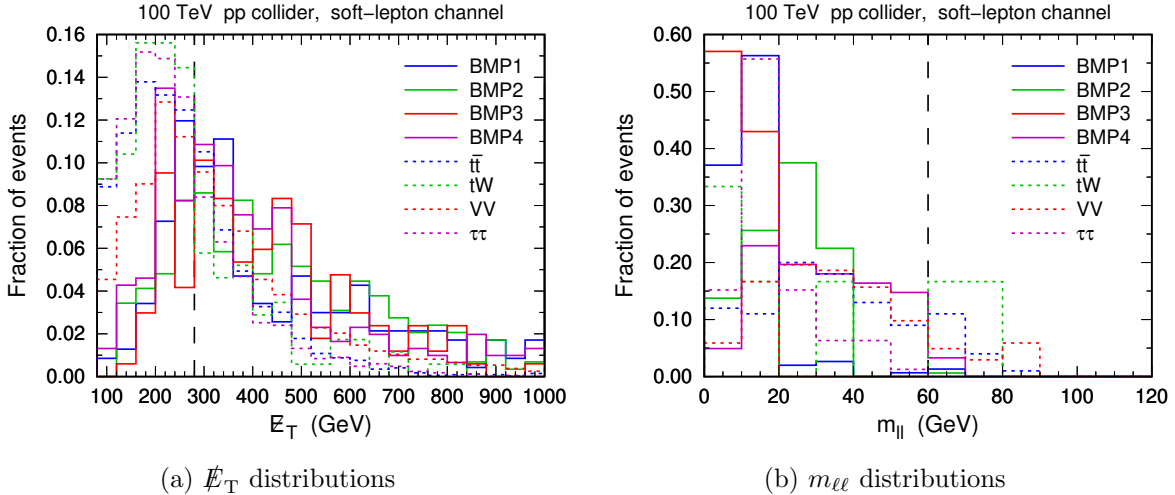


FIG. 6. Fraction of signal and background events binned in  $\cancel{E}_T$  after cut 3 (a) and in  $m_{\ell\ell}$  after cut 5 (b) in the soft-leptons + jets +  $\cancel{E}_T$  channel at a 100 TeV  $pp$  collider. Dashed lines indicate the cut thresholds.

the  $m_{\tau\tau}$  distribution of the  $\tau^+\tau^- + \text{jets}$  background peaks around  $m_Z$ , as demonstrated in Fig. 5(b). Additionally, the  $VV + \text{jets}$  distribution peaks around  $2m_W$  because of the  $W^+W^- \rightarrow \tau^+\tau^-\nu_\tau\bar{\nu}_\tau$  decay process. Therefore, a veto on the events with  $m_{\tau\tau} \in [0, 200]$  GeV in cut 3 can significantly suppress the  $\tau^+\tau^- + \text{jets}$  and  $VV + \text{jets}$  backgrounds.

Figure 6(a) presents the  $\cancel{E}_T$  distributions after applying cut 3. We find that the signal distributions are typically harder than the backgrounds, because the DM candidate  $\phi$  with a mass of  $\mathcal{O}(10^2)$  GeV induces larger  $\cancel{E}_T$  than neutrinos. Thus, we adopt the condition  $\cancel{E}_T > 280$  GeV in cut 4 to increase the signal significance. Cut 5 and cut 6 make use of the  $\cancel{E}_T/H_T^{\text{lep}}$  and  $m_{\ell\ell}$  variables, following the ATLAS analysis [71].

The  $m_{\ell\ell}$  distributions after applying cut 5 are displayed in Fig. 6(b). Inferring from Table IV, we have  $m_a - m_\phi \sim 20, 39, 16, 69$  GeV for BMP1, BMP2, BMP3, and BMP4, respectively. Such a difference in the mass splitting results in different end points in the  $m_{\ell\ell}$  distributions, as clearly shown in Fig. 6(b). Seven signal regions are defined by the  $m_{\ell\ell}$  bins as the same as those in Table III. Different  $m_{\ell\ell}$  bins would be suitable for different mass splittings.

Table VI lists the visible cross section and the signal significance for an integrated luminosity of  $3 \text{ ab}^{-1}$  after applying each cut in SR3. We can see that the signal significances of the four BMPs subsequently increase from cut 1 to cut 5. The cut condition  $m_{\ell\ell} \in [1, 3] \cup [3.2, 10]$  GeV in SR3 increase the significances of BMP1 and BMP3, but decrease those of BMP2 and BMP4. This is because BMP1 and BMP3 have smaller mass splittings and hence sufficient fractions of events satisfying  $m_{\ell\ell} \leq 10$  GeV, while BMP2 and BMP4 do not, as shown in Fig. 6(b). Larger  $m_{\ell\ell}$  bins in SR6 and SR7 would be applicable for BMP2 and BMP4.

Figure 7 shows the 95% CL expected exclusion region combing the seven signal regions at

TABLE VI. Visible cross section  $\sigma_{\text{vis}}$  in fb and signal significance  $\mathcal{S}$  for integrated luminosity  $3 \text{ ab}^{-1}$  after each cuts in SR3 of the soft-leptons + jets +  $\cancel{E}_T$  channel.

	$t\bar{t}$	$tW$	$VV$	$\tau\tau$	BMP1		BMP2		BMP3		BMP4	
	$\sigma_{\text{vis}}$	$\sigma_{\text{vis}}$	$\sigma_{\text{vis}}$	$\sigma_{\text{vis}}$	$\sigma_{\text{vis}}$	$\mathcal{S}$	$\sigma_{\text{vis}}$	$\mathcal{S}$	$\sigma_{\text{vis}}$	$\mathcal{S}$	$\sigma_{\text{vis}}$	$\mathcal{S}$
Cut1	37600	28400	5070	5420	1.53	0.303	2.29	0.453	0.618	0.122	17.3	3.43
Cut2	1790	296	804	510	0.625	0.586	0.770	0.722	0.262	0.246	5.77	5.42
Cut3	1280	232	383	73.3	0.567	0.699	0.669	0.825	0.243	0.300	4.61	5.68
Cut4	445	69.7	190	21.7	0.426	0.863	0.531	1.08	0.201	0.408	3.14	6.35
Cut5	37.3	8.04	9.91	3.47	0.366	2.57	0.368	2.59	0.185	1.30	0.934	6.50
SR3	4.11	2.68	0.583	0.528	0.136	2.59	0.0483	0.921	0.106	2.02	0.0455	0.868

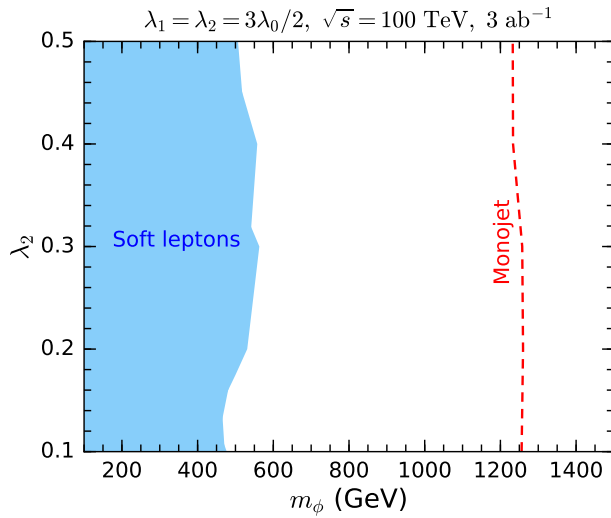


FIG. 7. 95% C.L. expected exclusion region in the soft-leptons + jets +  $\cancel{E}_T$  channel at a 100 TeV  $pp$  collider with an integrated luminosity of  $3 \text{ ab}^{-1}$  for the fixed coupling relation  $\lambda_1 = \lambda_2 = 3\lambda_0/2$ . For comparison, the red dashed line denotes the 95% C.L. expected exclusion limit in the monojet +  $\cancel{E}_T$  channel with the same collision energy and integrated luminosity.

a 100 TeV  $pp$  collider with a data set of  $3 \text{ ab}^{-1}$  for the fixed coupling relation  $\lambda_1 = \lambda_2 = 3\lambda_0/2$ . We find that the soft-leptons + jets +  $\cancel{E}_T$  channel can explore a region up to  $m_\phi \sim 550 \text{ GeV}$ . Nonetheless, such a sensitivity is not better than that in the monojet +  $\cancel{E}_T$  channel, which is demonstrated by the red dashed line.

## VI. CONCLUSIONS AND DISCUSSIONS

In this paper, we discuss the QSDM model, where the dark sector contains an inert  $\text{SU}(2)_L$  quadruplet scalar with  $Y = 1/2$ . After the electroweak symmetry breaking, there are one doubly charged scalar, two singly charged scalars, and two neutral scalars. For  $\lambda_2 > 0$ , the lighter neutral scalar  $\phi$  plays the role of DM particle. We have identified the

parameter regions that can predict an observed DM relic abundance.

As the DM candidate can interact with nucleons through the SM Higgs portal, direct detection experiments could be sensitive to this model. We have investigated the constraints from the current experiment XENON1T as well as the sensitivity of the future LZ experiment. Nonetheless, the  $h\phi\phi$  coupling could vanish if the quartic couplings  $\lambda_0$ ,  $\lambda_1$ , and  $\lambda_2$  satisfy special relations, resulting in null signal in direct detection. In this case, other types of DM search experiments would be essentially important.

Since the dark sector scalars carry electroweak charges, they could be directly produced in pairs at high energy  $pp$  colliders. The mass splittings among the dark sector scalars are typically lower than  $m_W$  and  $m_Z$ . As a result, the sensitive search channels at the LHC include the monojet +  $\cancel{E}_T$  and soft-leptons + jets +  $\cancel{E}_T$  channels. We have recast the ATLAS analyses in these two channels with  $\sqrt{s} = 13$  TeV and an integrated luminosity of  $36.1 \text{ fb}^{-1}$ . We have found that the monojet search have excluded some parameter regions up to  $m_\phi \sim 45$  GeV, while the soft-lepton channel has excluded larger regions up to  $m_\phi \sim 85$  GeV.

As these LHC constraints on the QSDM model still seem rather weak, we have studied the prospect of a future 100 TeV  $pp$  collider, either SPPC or FCC-hh. We have found that the monojet channel could be sensitive to the model up to  $m_\phi \sim 1.2$  TeV assuming an integrated luminosity of  $3 \text{ ab}^{-1}$ . On the other hand, the soft-lepton channel is less sensitive, reaching up to  $m_\phi \sim 550$  GeV.

Electroweak precision measurements provide an indirect probe to the QSDM model. In our previous study [19], we find that the future determination of electroweak oblique parameters in the Circular Electron Positron Collider project [73] would be able to reach up to  $m_\phi \sim 700$  GeV. Therefore, the direct search in the monojet channel at a 100 TeV  $pp$  collider seems more sensitive to the model.

## ACKNOWLEDGMENTS

This work is supported in part by the National Natural Science Foundation of China under Grants No. 11805288, No. 11875327, and No. 11905300, the China Postdoctoral Science Foundation under Grant No. 2018M643282, the Natural Science Foundation of Guangdong Province under Grant No. 2016A030313313, the Fundamental Research Funds for the Central Universities, and the Sun Yat-Sen University Science Foundation.

### Appendix A: Electroweak Gauge Interactions of the Quadruplet Scalar

The generators in the  $SU(2)_L$  representation **4** are given by

$$T^1 = \begin{pmatrix} & \sqrt{3}/2 & & \\ \sqrt{3}/2 & & 1 & \\ & 1 & & \sqrt{3}/2 \\ & & \sqrt{3}/2 & \end{pmatrix}, \quad T^2 = \begin{pmatrix} & -\sqrt{3}i/2 & & \\ \sqrt{3}i/2 & & -i & \\ & i & & -\sqrt{3}i/2 \\ & & \sqrt{3}i/2 & \end{pmatrix},$$

$$T^3 = \text{diag} \left( \frac{3}{2}, \frac{1}{2}, -\frac{1}{2}, -\frac{3}{2} \right). \quad (\text{A1})$$

Utilizing these generators, we can expand the gauge interaction terms for the quadruplet scalar as

$$\begin{aligned} \mathcal{L}_{\text{gauge}} = & g \left[ \frac{\sqrt{6}}{2} W_\mu^+ (X^{++})^* i \overleftrightarrow{\partial}^\mu X^+ + \sqrt{2} W_\mu^+ (X^+)^* i \overleftrightarrow{\partial}^\mu X^0 + \frac{\sqrt{6}}{2} W_\mu^+ (X^0)^* i \overleftrightarrow{\partial}^\mu X^- + \text{H.c.} \right] \\ & + e A_\mu \left[ 2(X^{++})^* i \overleftrightarrow{\partial}^\mu X^{++} + (X^+)^* i \overleftrightarrow{\partial}^\mu X^+ - (X^-)^* i \overleftrightarrow{\partial}^\mu X^- \right] \\ & + \frac{g}{2c_W} Z_\mu \left[ (3c_W^2 - s_W^2)(X^{++})^* i \overleftrightarrow{\partial}^\mu X^{++} + (c_W^2 - s_W^2)(X^+)^* i \overleftrightarrow{\partial}^\mu X^+ \right. \\ & \quad \left. + i a i \overleftrightarrow{\partial}^\mu \phi - (3c_W^2 + s_W^2)(X^-)^* i \overleftrightarrow{\partial}^\mu X^- \right] \\ & + \frac{g^2}{2} W_\mu^+ W^{-\mu} [3|X^{++}|^2 + 7|X^+|^2 + 7|X^0|^2 + 3|X^-|^2] \\ & + g^2 \left[ \sqrt{3} W_\mu^+ W^{+\mu} (X^{++})^* X^0 + \sqrt{3} W_\mu^+ W^{+\mu} (X^+)^* X^- + \text{H.c.} \right] \\ & + e^2 A_\mu A^\mu (4|X^{++}|^2 + |X^+|^2 + |X^-|^2) \\ & + \frac{eg}{c_W} A_\mu Z^\mu [2(3c_W^2 - s_W^2)|X^{++}|^2 + (c_W^2 - s_W^2)|X^+|^2 + (3c_W^2 + s_W^2)|X^-|^2] \\ & + \frac{g^2}{4c_W^2} Z_\mu Z^\mu [(3c_W^2 - s_W^2)^2 |X^{++}|^2 + (c_W^2 - s_W^2)^2 |X^+|^2 + |X^0|^2 + (3c_W^2 + s_W^2)^2 |X^-|^2] \\ & + \left\{ \left[ \frac{3\sqrt{6}}{2} eg A^\mu + \frac{\sqrt{6}g^2(2c_W^2 - s_W^2)}{2c_W} Z^\mu \right] W_\mu^+ (X^{++})^* X^+ \right. \\ & \quad + \left( \sqrt{2} eg A^\mu - \frac{\sqrt{2}g^2 s_W^2}{c_W} Z^\mu \right) W_\mu^+ (X^+)^* X^0 \\ & \quad \left. - \left[ \frac{\sqrt{6}}{2} eg A^\mu + \frac{\sqrt{6}g^2(2c_W^2 + s_W^2)}{2c_W} Z^\mu \right] W_\mu^+ (X^0)^* X^- + \text{H.c.} \right\}. \quad (\text{A2}) \end{aligned}$$

Here  $c_W \equiv \cos \theta_W$  and  $s_W \equiv \sin \theta_W$ , where  $\theta_W = \tan^{-1}(g'/g)$  is the weak mixing angle.

- 
- [1] G. Bertone, D. Hooper, and J. Silk, “Particle dark matter: Evidence, candidates and constraints,” *Phys. Rept.* **405** (2005) 279–390, [arXiv:hep-ph/0404175 \[hep-ph\]](#).
  - [2] J. L. Feng, “Dark Matter Candidates from Particle Physics and Methods of Detection,” *Ann. Rev. Astron. Astrophys.* **48** (2010) 495–545, [arXiv:1003.0904 \[astro-ph.CO\]](#).
  - [3] B.-L. Young, “A survey of dark matter and related topics in cosmology,” *Front. Phys.(Beijing)* **12** (2017) 121201. [Erratum: *Front. Phys.(Beijing)*12,no.2,121202(2017)].
  - [4] R. Mahbubani and L. Senatore, “The Minimal model for dark matter and unification,” *Phys. Rev.* **D73** (2006) 043510, [arXiv:hep-ph/0510064 \[hep-ph\]](#).
  - [5] M. Cirelli, N. Fornengo, and A. Strumia, “Minimal dark matter,” *Nucl. Phys.* **B753** (2006) 178–194, [arXiv:hep-ph/0512090 \[hep-ph\]](#).
  - [6] T. Hambye, F. S. Ling, L. Lopez Honorez, and J. Rocher, “Scalar Multiplet Dark Matter,” *JHEP* **07** (2009) 090, [arXiv:0903.4010 \[hep-ph\]](#). [Erratum: *JHEP*05,066(2010)].
  - [7] T. Cohen, J. Kearney, A. Pierce, and D. Tucker-Smith, “Singlet-Doublet Dark Matter,” *Phys. Rev.* **D85** (2012) 075003, [arXiv:1109.2604 \[hep-ph\]](#).
  - [8] Y. Cai, W. Chao, and S. Yang, “Scalar Septuplet Dark Matter and Enhanced  $h \rightarrow \gamma\gamma$  Decay Rate,” *JHEP* **12** (2012) 043, [arXiv:1208.3949 \[hep-ph\]](#).
  - [9] K. Earl, K. Hartling, H. E. Logan, and T. Pilkington, “Constraining models with a large scalar multiplet,” *Phys. Rev.* **D88** (2013) 015002, [arXiv:1303.1244 \[hep-ph\]](#).
  - [10] S. S. AbdusSalam and T. A. Chowdhury, “Scalar Representations in the Light of Electroweak Phase Transition and Cold Dark Matter Phenomenology,” *JCAP* **1405** (2014) 026, [arXiv:1310.8152 \[hep-ph\]](#).
  - [11] O. Fischer and J. J. van der Bij, “The scalar Singlet-Triplet Dark Matter Model,” *JCAP* **1401** (2014) 032, [arXiv:1311.1077 \[hep-ph\]](#).
  - [12] A. Dedes and D. Karamitros, “Doublet-Triplet Fermionic Dark Matter,” *Phys. Rev.* **D89** (2014) 115002, [arXiv:1403.7744 \[hep-ph\]](#).
  - [13] B. Ostdiek, “Constraining the minimal dark matter fiveplet with LHC searches,” *Phys. Rev.* **D92** (2015) 055008, [arXiv:1506.03445 \[hep-ph\]](#).
  - [14] C. Cai, Z.-M. Huang, Z. Kang, Z.-H. Yu, and H.-H. Zhang, “Perturbativity Limits for Scalar Minimal Dark Matter with Yukawa Interactions: Septuplet,” *Phys. Rev.* **D92** (2015) 115004, [arXiv:1510.01559 \[hep-ph\]](#).
  - [15] T. M. P. Tait and Z.-H. Yu, “Triplet-Quadruplet Dark Matter,” *JHEP* **03** (2016) 204, [arXiv:1601.01354 \[hep-ph\]](#).
  - [16] S. Banerjee, S. Matsumoto, K. Mukaida, and Y.-L. S. Tsai, “WIMP Dark Matter in a Well-Tempered Regime: A case study on Singlet-Doublets Fermionic WIMP,” *JHEP* **11** (2016) 070, [arXiv:1603.07387 \[hep-ph\]](#).

- [17] W.-B. Lu and P.-H. Gu, “Mixed Inert Scalar Triplet Dark Matter, Radiative Neutrino Masses and Leptogenesis,” *Nucl. Phys.* **B924** (2017) 279–311, [arXiv:1611.02106 \[hep-ph\]](#).
- [18] C. Cai, Z.-H. Yu, and H.-H. Zhang, “CEPC Precision of Electroweak Oblique Parameters and Weakly Interacting Dark Matter: the Fermionic Case,” *Nucl. Phys.* **B921** (2017) 181–210, [arXiv:1611.02186 \[hep-ph\]](#).
- [19] C. Cai, Z.-H. Yu, and H.-H. Zhang, “CEPC Precision of Electroweak Oblique Parameters and Weakly Interacting Dark Matter: the Scalar Case,” *Nucl. Phys.* **B924** (2017) 128–152, [arXiv:1705.07921 \[hep-ph\]](#).
- [20] X. Liu and L. Bian, “Dark matter and electroweak phase transition in the mixed scalar dark matter model,” *Phys. Rev.* **D97** (2018) 055028, [arXiv:1706.06042 \[hep-ph\]](#).
- [21] Q.-F. Xiang, X.-J. Bi, P.-F. Yin, and Z.-H. Yu, “Exploring Fermionic Dark Matter via Higgs Boson Precision Measurements at the Circular Electron Positron Collider,” *Phys. Rev.* **D97** (2018) 055004, [arXiv:1707.03094 \[hep-ph\]](#).
- [22] C. Cai, Z. Kang, Z. Luo, Z.-H. Yu, and H.-H. Zhang, “Scalar quintuplet minimal dark matter with Yukawa interactions: perturbative up to the Planck scale,” *Chin. Phys.* **C43** (2019) 023102, [arXiv:1711.07396 \[hep-ph\]](#).
- [23] L. Lopez Honorez, M. H. G. Tytgat, P. Tziveloglou, and B. Zaldivar, “On Minimal Dark Matter coupled to the Higgs,” *JHEP* **04** (2018) 011, [arXiv:1711.08619 \[hep-ph\]](#).
- [24] C. Cai, Z. Kang, H.-H. Zhang, and Y.-P. Zeng, “Minimal dark matter in  $SU(2)_L \times U(1)_Y \times U(1)_{B-L}$ ,” *Phys. Lett.* **B784** (2018) 385–391, [arXiv:1801.05594 \[hep-ph\]](#).
- [25] A. Dutta Banik, A. K. Saha, and A. Sil, “Scalar assisted singlet doublet fermion dark matter model and electroweak vacuum stability,” *Phys. Rev.* **D98** (2018) 075013, [arXiv:1806.08080 \[hep-ph\]](#).
- [26] P.-H. Gu and H.-J. He, “TeV Scale Neutrino Mass Generation, Minimal Inelastic Dark Matter, and High Scale Leptogenesis,” *Phys. Rev.* **D99** (2019) 015025, [arXiv:1808.09377 \[hep-ph\]](#).
- [27] A. Betancur and Ó. Zapata, “Phenomenology of doublet-triplet fermionic dark matter in nonstandard cosmology and multicomponent dark sectors,” *Phys. Rev.* **D98** (2018) 095003, [arXiv:1809.04990 \[hep-ph\]](#).
- [28] K. Kadota and A. Spray, “Electroweak Multiplet Dark Matter at Future Lepton Colliders,” *JHEP* **02** (2019) 017, [arXiv:1811.00560 \[hep-ph\]](#).
- [29] J.-W. Wang, X.-J. Bi, P.-F. Yin, and Z.-H. Yu, “Impact of Fermionic Electroweak Multiplet Dark Matter on Vacuum Stability with One-loop Matching,” *Phys. Rev.* **D99** (2019) 055009, [arXiv:1811.08743 \[hep-ph\]](#).
- [30] A. Filimonova and S. Westhoff, “Long live the Higgs portal!,” *JHEP* **02** (2019) 140, [arXiv:1812.04628 \[hep-ph\]](#).

- [31] W. Chao, G.-J. Ding, X.-G. He, and M. Ramsey-Musolf, “Scalar Electroweak Multiplet Dark Matter,” *JHEP* **08** (2019) 058, [arXiv:1812.07829 \[hep-ph\]](#).
- [32] T. Abe and R. Sato, “Current status and future prospects of the singlet-doublet dark matter model with CP-violation,” *Phys. Rev.* **D99** (2019) 035012, [arXiv:1901.02278 \[hep-ph\]](#).
- [33] Y. Cheng and W. Liao, “Fate of false vacuum in a singlet-doublet dark matter model with RG improved effective action,” [arXiv:1909.11941 \[hep-ph\]](#).
- [34] N. G. Deshpande and E. Ma, “Pattern of Symmetry Breaking with Two Higgs Doublets,” *Phys. Rev.* **D18** (1978) 2574.
- [35] R. Barbieri, L. J. Hall, and V. S. Rychkov, “Improved naturalness with a heavy Higgs: An Alternative road to LHC physics,” *Phys. Rev.* **D74** (2006) 015007, [arXiv:hep-ph/0603188 \[hep-ph\]](#).
- [36] M. Gustafsson, E. Lundstrom, L. Bergstrom, and J. Edsjo, “Significant Gamma Lines from Inert Higgs Dark Matter,” *Phys. Rev. Lett.* **99** (2007) 041301, [arXiv:astro-ph/0703512 \[ASTRO-PH\]](#).
- [37] Q.-H. Cao, E. Ma, and G. Rajasekaran, “Observing the Dark Scalar Doublet and its Impact on the Standard-Model Higgs Boson at Colliders,” *Phys. Rev.* **D76** (2007) 095011, [arXiv:0708.2939 \[hep-ph\]](#).
- [38] P. Fileviez Perez, H. H. Patel, M. Ramsey-Musolf, and K. Wang, “Triplet Scalars and Dark Matter at the LHC,” *Phys. Rev.* **D79** (2009) 055024, [arXiv:0811.3957 \[hep-ph\]](#).
- [39] T. Araki, C. Q. Geng, and K. I. Nagao, “Dark Matter in Inert Triplet Models,” *Phys. Rev.* **D83** (2011) 075014, [arXiv:1102.4906 \[hep-ph\]](#).
- [40] F.-X. Josse-Michaux and E. Molinaro, “Triplet scalar dark matter and leptogenesis in an inverse seesaw model of neutrino mass generation,” *Phys. Rev.* **D87** (2013) 036007, [arXiv:1210.7202 \[hep-ph\]](#).
- [41] S. Yaser Ayazi and S. M. Firouzabadi, “Constraining Inert Triplet Dark Matter by the LHC and FermiLAT,” *JCAP* **1411** (2014) 005, [arXiv:1408.0654 \[hep-ph\]](#).
- [42] N. Khan, “Exploring the hyperchargeless Higgs triplet model up to the Planck scale,” *Eur. Phys. J.* **C78** (2018) 341, [arXiv:1610.03178 \[hep-ph\]](#).
- [43] M. Beltran, D. Hooper, E. W. Kolb, Z. A. C. Krusberg, and T. M. P. Tait, “Maverick dark matter at colliders,” *JHEP* **09** (2010) 037, [arXiv:1002.4137 \[hep-ph\]](#).
- [44] A. Rajaraman, W. Shepherd, T. M. P. Tait, and A. M. Wijangco, “LHC Bounds on Interactions of Dark Matter,” *Phys. Rev.* **D84** (2011) 095013, [arXiv:1108.1196 \[hep-ph\]](#).
- [45] P. J. Fox, R. Harnik, J. Kopp, and Y. Tsai, “Missing Energy Signatures of Dark Matter at the LHC,” *Phys. Rev.* **D85** (2012) 056011, [arXiv:1109.4398 \[hep-ph\]](#).
- [46] Z.-H. Yu, X.-J. Bi, Q.-S. Yan, and P.-F. Yin, “Detecting light stop pairs in coannihilation scenarios at the LHC,” *Phys. Rev.* **D87** (2013) 055007, [arXiv:1211.2997 \[hep-ph\]](#).
- [47] Q.-F. Xiang, X.-J. Bi, P.-F. Yin, and Z.-H. Yu, “Searches for dark matter signals in simplified models at future hadron colliders,” *Phys. Rev.* **D91** (2015) 095020,

- [arXiv:1503.02931 \[hep-ph\]](#).
- [48] J.-W. Wang, X.-J. Bi, Q.-F. Xiang, P.-F. Yin, and Z.-H. Yu, “Exploring triplet-quadruplet fermionic dark matter at the LHC and future colliders,” *Phys. Rev.* **D97** (2018) 035021, [arXiv:1711.05622 \[hep-ph\]](#).
- [49] G. F. Giudice, T. Han, K. Wang, and L.-T. Wang, “Nearly Degenerate Gauginos and Dark Matter at the LHC,” *Phys. Rev.* **D81** (2010) 115011, [arXiv:1004.4902 \[hep-ph\]](#).
- [50] S. Gori, S. Jung, and L.-T. Wang, “Cornering electroweakinos at the LHC,” *JHEP* **10** (2013) 191, [arXiv:1307.5952 \[hep-ph\]](#).
- [51] P. Schwaller and J. Zurita, “Compressed electroweakino spectra at the LHC,” *JHEP* **03** (2014) 060, [arXiv:1312.7350 \[hep-ph\]](#).
- [52] Z. Han, G. D. Kribs, A. Martin, and A. Menon, “Hunting quasidegenerate Higgsinos,” *Phys. Rev.* **D89** (2014) 075007, [arXiv:1401.1235 \[hep-ph\]](#).
- [53] H. Baer, A. Mustafayev, and X. Tata, “Monojet plus soft dilepton signal from light higgsino pair production at LHC14,” *Phys. Rev.* **D90** (2014) 115007, [arXiv:1409.7058 \[hep-ph\]](#).
- [54] **CEPC-SPPC Study Group** Collaboration, M. Ahmad *et al.*, “CEPC-SPPC Preliminary Conceptual Design Report. 1. Physics and Detector,” IHEP-CEPC-DR-2015-01, IHEP-TH-2015-01, IHEP-EP-2015-01.
- [55] **FCC** Collaboration, A. Abada *et al.*, “FCC Physics Opportunities,” *Eur. Phys. J.* **C79** (2019) 474.
- [56] A. Belyaev, G. Cacciapaglia, I. P. Ivanov, F. Rojas-Abatte, and M. Thomas, “Anatomy of the Inert Two Higgs Doublet Model in the light of the LHC and non-LHC Dark Matter Searches,” *Phys. Rev.* **D97** (2018) 035011, [arXiv:1612.00511 \[hep-ph\]](#).
- [57] K. Griest and D. Seckel, “Three exceptions in the calculation of relic abundances,” *Phys. Rev.* **D43** (1991) 3191–3203.
- [58] A. Alloul, N. D. Christensen, C. Degrande, C. Duhr, and B. Fuks, “FeynRules 2.0 - A complete toolbox for tree-level phenomenology,” *Comput. Phys. Commun.* **185** (2014) 2250–2300, [arXiv:1310.1921 \[hep-ph\]](#).
- [59] J. Alwall, R. Frederix, S. Frixione, V. Hirschi, F. Maltoni, O. Mattelaer, H. S. Shao, T. Stelzer, P. Torrielli, and M. Zaro, “The automated computation of tree-level and next-to-leading order differential cross sections, and their matching to parton shower simulations,” *JHEP* **07** (2014) 079, [arXiv:1405.0301 \[hep-ph\]](#).
- [60] F. Ambrogio, C. Arina, M. Backovic, J. Heisig, F. Maltoni, L. Mantani, O. Mattelaer, and G. Mohlabeng, “MadDM v.3.0: a Comprehensive Tool for Dark Matter Studies,” *Phys. Dark Univ.* **24** (2019) 100249, [arXiv:1804.00044 \[hep-ph\]](#).
- [61] **Planck** Collaboration, N. Aghanim *et al.*, “Planck 2018 results. VI. Cosmological parameters,” [arXiv:1807.06209 \[astro-ph.CO\]](#).
- [62] **XENON** Collaboration, E. Aprile *et al.*, “Dark Matter Search Results from a One Ton-Year Exposure of XENON1T,” *Phys. Rev. Lett.* **121** (2018) 111302, [arXiv:1805.12562](#)

- [astro-ph.CO].
- [63] B. J. Mount *et al.*, “LUX-ZEPLIN (LZ) Technical Design Report,” [arXiv:1703.09144](#) [[physics.ins-det](#)].
- [64] Z.-H. Yu, J.-M. Zheng, X.-J. Bi, Z. Li, D.-X. Yao, and H.-H. Zhang, “Constraining the interaction strength between dark matter and visible matter: II. scalar, vector and spin-3/2 dark matter,” *Nucl. Phys.* **B860** (2012) 115–151, [arXiv:1112.6052](#) [[hep-ph](#)].
- [65] J. R. Ellis, A. Ferstl, and K. A. Olive, “Reevaluation of the elastic scattering of supersymmetric dark matter,” *Phys. Lett.* **B481** (2000) 304–314, [arXiv:hep-ph/0001005](#) [[hep-ph](#)].
- [66] **ATLAS** Collaboration, M. Aaboud *et al.*, “Search for dark matter and other new phenomena in events with an energetic jet and large missing transverse momentum using the ATLAS detector,” *JHEP* **01** (2018) 126, [arXiv:1711.03301](#) [[hep-ex](#)].
- [67] T. Sjöstrand, S. Ask, J. R. Christiansen, R. Corke, N. Desai, P. Ilten, S. Mrenna, S. Prestel, C. O. Rasmussen, and P. Z. Skands, “An Introduction to PYTHIA 8.2,” *Comput. Phys. Commun.* **191** (2015) 159–177, [arXiv:1410.3012](#) [[hep-ph](#)].
- [68] M. L. Mangano, M. Moretti, F. Piccinini, and M. Treccani, “Matching matrix elements and shower evolution for top-quark production in hadronic collisions,” *JHEP* **01** (2007) 013, [arXiv:hep-ph/0611129](#) [[hep-ph](#)].
- [69] **DELPHES 3** Collaboration, J. de Favereau, C. Delaere, P. Demin, A. Giammanco, V. Lemaître, A. Mertens, and M. Selvaggi, “DELPHES 3, A modular framework for fast simulation of a generic collider experiment,” *JHEP* **02** (2014) 057, [arXiv:1307.6346](#) [[hep-ex](#)].
- [70] **ATLAS** Collaboration, M. Aaboud *et al.*, “Search for electroweak production of supersymmetric particles in final states with two or three leptons at  $\sqrt{s} = 13$  TeV with the ATLAS detector,” *Eur. Phys. J.* **C78** (2018) 995, [arXiv:1803.02762](#) [[hep-ex](#)].
- [71] **ATLAS** Collaboration, M. Aaboud *et al.*, “Search for electroweak production of supersymmetric states in scenarios with compressed mass spectra at  $\sqrt{s} = 13$  TeV with the ATLAS detector,” *Phys. Rev.* **D97** (2018) 052010, [arXiv:1712.08119](#) [[hep-ex](#)].
- [72] A. Barr and J. Scoville, “A boost for the EW SUSY hunt: monojet-like search for compressed sleptons at LHC14 with  $100 \text{ fb}^{-1}$ ,” *JHEP* **04** (2015) 147, [arXiv:1501.02511](#) [[hep-ph](#)].
- [73] **CEPC Study Group** Collaboration, M. Dong *et al.*, “CEPC Conceptual Design Report: Volume 2 - Physics & Detector,” [arXiv:1811.10545](#) [[hep-ex](#)].